GDCh Research Article Angewandte International Edition Chemie www.angewandte.org

How to cite: *Angew. Chem. Int. Ed.* **2025**, *64*, e202505212
doi.org/10.1002/anie.202505212

Batteries

Data–Knowledge-Dual-Driven Electrolyte Design for Fast-Charging Lithium Ion Batteries

Yi Yang, Nan Yao, Yu-Chen Gao, Xiang Chen, Yu-Xin Huang, Shuo Zhang, Han-Bing Zhu, Lei Xu, Yu-Xing Yao, Shi-Jie Yang, Zheng Liao, Zeheng Li, Xue-Fei Wen, Peng Wu, Ting-Lu Song, Jin-Hao Yao, Jiang-Kui Hu, Chong Yan, Jia-Qi Huang,* and Qiang Zhang**

Abstract: Electric vehicles (EVs) starve for minutes-level fast-charging lithium-ion batteries (LIBs), while the heat gathering at high-rate charging and torridity conditions has detrimental effects on electrolytes, triggering rapid battery degradation and even safety hazards. However, the current research on high-temperature fast-charging (HTFC) electrolytes is very lacking. We revolutionized the conventional paradigm of developing HTFC electrolytes integrating with high-throughput calculation, machine-learning techniques, and experimental verifications to establish a data–knowledge-dual-driven approach. Ethyl trimethylacetate was efficiently screened out based on the approach and enabled batteries to work under high temperatures with distinctly restricted side reactions. A stable and highly safe fast-charging (15-min charging to 80% capacity) cycling without Li plating was achieved over 4100 cycles at 45 °C based on 181 Wh kg^{-1} pouch cells, demonstrating the state-of-the-art in this field.

Introduction

Accompanying the green and environmentally friendly advantages of electric vehicles (EVs) is the drawback of their slow electric refueling rate and the resulting range anxiety.[1–4] These all underscore the importance of reducing battery charging time with fast-charging technology, which can boost electric transportation with convenience and efficiency.[4–9] The current fast-charging technology allows for batteries to charge at high rates, such as 4.0–6.0 C, namely charging to 80% capacity within 10–15 min.[10–14] Excessive charging rates will increase battery temperature during charging. Specifically, the battery temperature increased by approximately 24 °C in a 10-min fast-charging protocol, and the increment even reached up to 270 °C at the pack level.[15,16] In addition to the hyperthermia during fast charging, lithium-ion batteries (LIBs) utilized in mining and military are also subjected to extreme high temperatures (>80 °C).[17] Meanwhile, numerous countries are currently facing harsh heatwaves, which pose increasingly stringent challenges to the high-temperature stability of LIBs.[18] Moreover, the heat-resistant LIBs will simplify the thermal management system of the battery (temperature-gradient-driven heat dissipation), which can reduce the cooling energy consumption and cost of the battery, but also improve the volume utilization efficiency and energy density of the battery pack.[19,20]

Among battery components, electrolyte is the most susceptible to elevated temperatures. A high temperature can expedite the electrolyte degradation, deteriorate the electrochemical performance, shorten the lifespan, and increase the hazards of gas production and the danger of thermal runaway, consequently compromising battery safety.[21] The profound effects of the electrolyte on the fast chargeability and thermal safety of LIBs were highlighted in numerous studies.[22,23] The electrolyte is inextricably related to the lithium-ion (Li^+) migration in the bulk electrolyte, the desolvation of the Li^+ at the electrode–electrolyte interface, and the Li^+ transport across the solid electrolyte interphase (SEI), which are considered pivotal steps in determining the battery's fast-charging performance.[14,24–27] The thermal stability of

[*] Y. Yang, S. Zhang, L. Xu, S.-J. Yang, Z. Liao, T.-L. Song, J.-K. Hu, C. Yan, J.-Q. Huang
School of Materials Science and Engineering, Beijing Institute of Technology, Beijing 100081, P.R. China
E-mail: jqhuang@bit.edu.cn

Y. Yang, S. Zhang, L. Xu, S.-J. Yang, Z. Liao, J.-K. Hu, C. Yan, J.-Q. Huang
Advanced Research Institute of Multidisciplinary Science, Beijing Institute of Technology, Beijing 100081, P.R. China

Y. Yang, N. Yao, Y.-C. Gao, X. Chen, Y.-X. Huang, H.-B. Zhu, Y.-X. Yao, Z. Li, J.-H. Yao, J.-K. Hu, Q. Zhang
Beijing Key Laboratory of Complex Solid State Batteries, Tsinghua Center for Green Chemical Engineering Electrification, Department of Chemical Engineering, Tsinghua University, Beijing 100084, P.R. China
E-mail: xiangchen@tsinghua.edu.cn
zhang-qiang@mails.tsinghua.edu.cn

Z. Li
College of Chemical and Biological Engineering, Zhejiang University, Hangzhou 310058, P.R. China

X.-F. Wen, P. Wu, C. Yan, Q. Zhang
Shanxi Research Institute for Clean Energy, Tsinghua University, Taiyuan 030032, P.R. China

Q. Zhang
Institute for Carbon Neutrality, Tsinghua University, Beijing 100084, P.R. China

Additional supporting information can be found online in the Supporting Information section

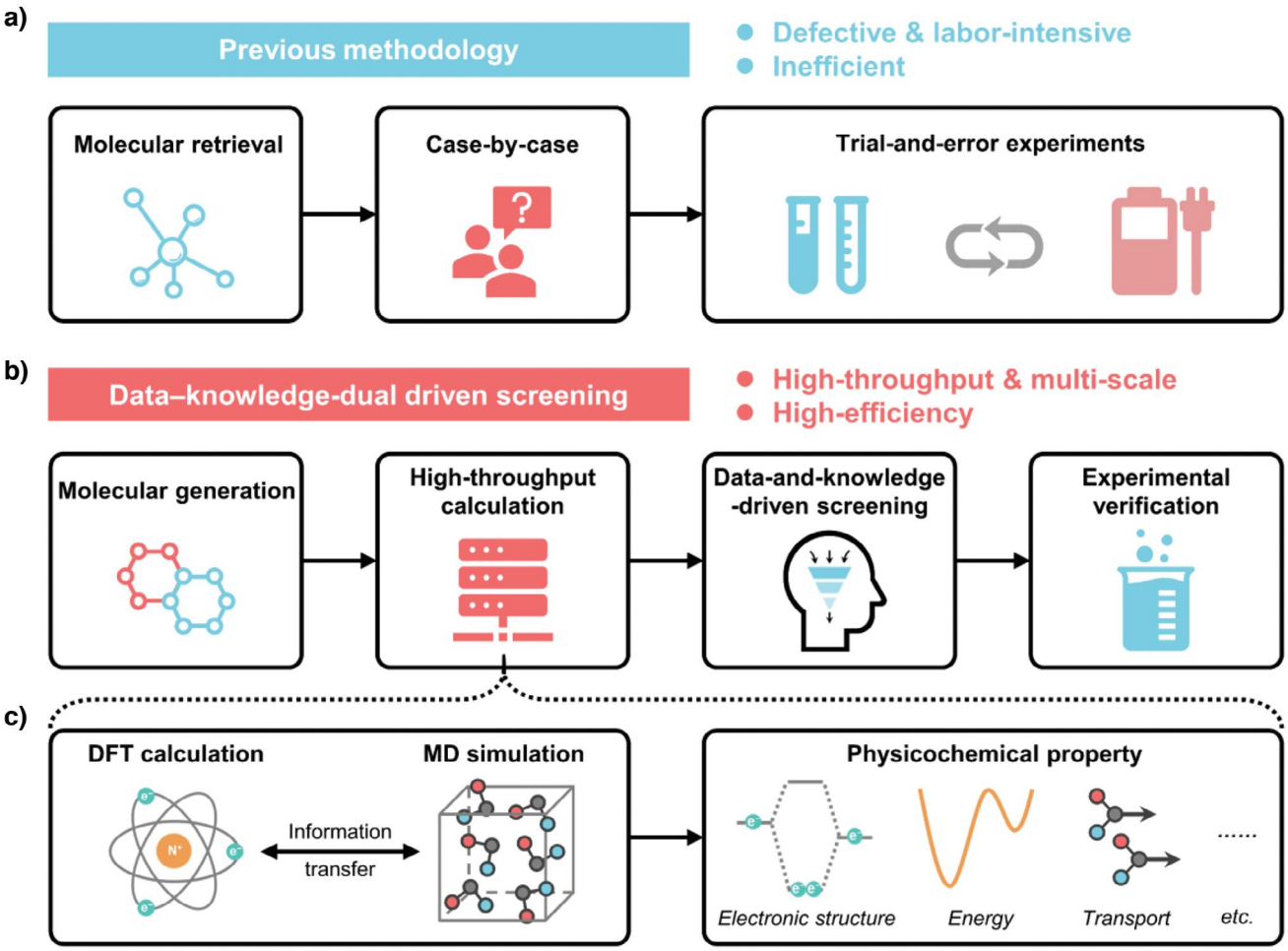

Figure 1. Past and data–knowledge-dual-driven molecular mining framework. a) Previous methodology of the molecular screening involving three steps: Molecule retrieval within a limited range, investigation case-by-case, repetitive and inefficient trial-and-error experiments. b) and c) Data–knowledge-dual-driven molecular design involving four steps: the molecular generation, the high-throughput calculation c), the data-and-knowledge-driven screening, and the experimental verification.

electrolyte constituents and their decomposition products are closely linked to the thermal safety of batteries. Therefore, it is crucial to develop advanced electrolytes with high-temperature resistance and fast-charging capability to enable the stable and safe cycling of LIBs.[28,29]

The solvent is a primary constituent of the electrolyte. Its properties, such as solvating power, viscosity, chemical stability, and thermal stability, directly impact the ionic conductivity, electrode compatibility, SEI properties, and eventually the battery performance under high-temperature fast-charging (HTFC) operating conditions.[30,31] Consequently, the design and selection of solvents have garnered considerable research attention.[27,32–34] Nevertheless, the previous methodology of molecular design predominantly depends on a trial-and-error approach, wherein researchers test different formulations and analyze the resulting battery performance (Figure 1a). This method is complemented by a case-by-case analysis with finite molecular space to understand the specific properties and working mechanisms of each solvent molecule. Facing the multiobjective challenge of molecular design and a vast molecular space yet to be explored, the labor-intensive trial-and-error approach falls short of efficiently designing eligible solvents. Assistive-computational tools, such as high-throughput molecular modeling and machine learning (ML) methodologies, present hopeful solutions to this dilemma. Simulation-assisted molecule design enables the efficient determination of solvent properties and offers an in-depth understanding of molecular-level interactions, facilitating the comprehension of the fundamental mechanisms that regulate solvent behaviors. Combined with property prediction by ML models, it can achieve the screening of thousands of molecules in parallel, identifying those satisfying desired criteria without prior laboratory work. Leveraging these techniques and experimental validation is expected to accelerate the discovery process and propose optimal electrolyte solvent molecules with great accuracy and efficiency, ultimately enhancing the ability of LIBs to operate at HTFC conditions.

We construct a systematic data–knowledge-dual-driven molecular design framework integrating molecular generation, high-throughput calculation, data-and-knowledge-driven screening, and experimental verification (Figure 1b) toward the parameterized HTFC requirements (covering

molecular stability, liquid range, solvation ability, viscosity, side-reaction restraint and availability, etc.), which achieved great success in uncovering three novel carboxylate molecules (methyl trimethylacetate (MTMA), ethyl trimethylacetate (ETMA), and ethyl 2,2-dimethylbutanoate (EDMB)) from 1 321 129 molecules. The electrolytes of screened three carboxylates demonstrate an anodic potential window of over 5.2 V and remarkable stability in reduction compared with routine carbonate-based electrolytes (ethylene carbonate (EC) and dimethyl carbonate (DMC) electrolytes). Strikingly, the robust interphasial film derived from ETMA-based electrolyte distinctly prevent the side-reaction under high-temperature and enhance the Li-ion pouch cell delivering a splendid HTFC performance with intensifying thermal safety.

Results and Discussion

Molecular Design Framework

The data–knowledge-dual-driven framework of designing electrolyte molecules involves four steps: molecular generation, high-throughput calculation, data and knowledge dual-driven screening, and experimental verification. Prevalent solvents used in LIBs are organic compounds mainly composed of hydrogen (H), carbon (C), and oxygen (O) atoms.[35,36] Accordingly, a molecular structure dataset with less than 10 C and O atoms and no restriction of H atoms was generated by Surge tool.[37] As a result, the molecular dataset with 1 321 129 molecules was constructed. 54 202 of these molecules were randomly chosen in the following high-throughput computations, which include density functional theory (DFT) calculation and molecular dynamics (MD) simulation to acquire various molecular properties such as viscosity and solvation ability (Figure 1c). Assisted by ML models (molecular property prediction, in methods), the properties of all previously generated molecules were determined, forming a comprehensive electrolyte property database.[38] The database is available for subsequent screening, significantly promoting the efficiency of picking optimal electrolyte candidates in a high-throughput way.

The screening approach is customized based on the above database and domain knowledge to design solvent molecules for LIBs that can withstand high temperatures and enable fast charging (Figure 2a):

1. Thermal stability: The formation energy of each molecule becomes the first and foremost screening criterion as it indicates the intrinsic thermal stability. According to the formation energies of routine molecules used in LIB electrolytes (Figure S1), a threshold of −0.10 eV atom^{-1} was set. The molecules with higher formation energies than the threshold were filtered out, with less than 200 000 molecules remaining.

2. Structural stability: Applying molecules with high voltage stability to LIBs is the precondition. Molecules with ether functional groups, double or triple carbon bonds, and 3- or 4-membered rings have never taken the responsibility as main solvents for LIB electrolytes.[35,36] Accordingly, molecules possessing these structural characteristics (such as ether, unsaturated, and polycyclic carbonate molecules) were excluded and 2576 molecules remained for the next screening step.

3. Temperature range: High-temperature electrolytes require solvents with high boiling points to prevent vaporization, and low-temperature operation ought to be paid attention to simultaneously. Molecular melting points lower than 213.15 K while boiling points higher than 373.15 K were decided to establish a suitable operating temperature range for the electrolyte, outputting 249 molecules. In this step, most common carbonates were screened out, while carbonate molecules with high boiling points survived.

4. Solvation and viscosity: Weak Li^+–solvent interactions give rise to the facile desolvation of Li^+. In this case, anions are also prone to participate in the Li^+ solvation shell and decompose to form an inorganic-rich SEI. These all contribute to the improvement of fast chargeability. Additionally, viscous solvents and electrolytes are not preferred. As a result, 102 low-viscosity molecules with adequate solvating power that is neither too weak to achieve sufficient salt dissociation nor too strong to tackle fast charging were selected by referencing the binding energy of routine molecules with Li^+ (Figure S1).

5. Chemical stability: Side reactions and gas generation are especially severe under fast-charging and high-temperature conditions, where H• radicals are generated by molecular oxidation and will initiate flame propagation.[39] The generation of H• radicals is supposed to decrease the chemical stability of both molecule and electrolyte at high temperatures. Bond lengths between C and alpha-H (α-H) in molecules were analyzed to evaluate their breaking tendency. Bond lengths for α-H located at different sites generally exhibit an increasing trend in the sequence of H_O, $H_{w/o\,O}$, and H, suggesting a decline in chemical stability, which is consistent with the inductive effect of functional groups in organic chemistry (Figure S2). The average bond length of C─$H_{w/o\,O}$, that is, the group with moderate stability, was used as the upper limit to obtain a total of 64 stable molecules.

6. Inhibition of Mn dissolution: The dissolution of transition metal, represented by Mn, from cathode materials into the electrolyte is one of the immediate causes of battery degradation since the dissolved Mn^{2+} can transport from the cathode to the anode surface and destroy the SEI.[40,41] To alleviate such an effect, solvent molecules are supposed to possess a weak affinity to Mn^{2+}. In this case, the binding energy between Mn^{2+} and the above 64 molecules was calculated (Figure S3). Those molecules strongly binding to Mn^{2+} with a binding energy lower than −2.0 eV were excluded. 35 molecules (Table S1) proceed to the next step of screening.

7. Accessibility: Considering the convenience of experimental evaluation, molecules probably synthesizable or purchasable through the Chemical Abstracts Service (CAS) number were prioritized. 34 of 35 molecules are identified with a CAS number.

8. Cost: The costs of the above 34 molecules were finally considered. Economical chemicals are preferred during practical applications. Fourteen molecules passed the price limit of 20 CNY g^{-1} (Figure S4).

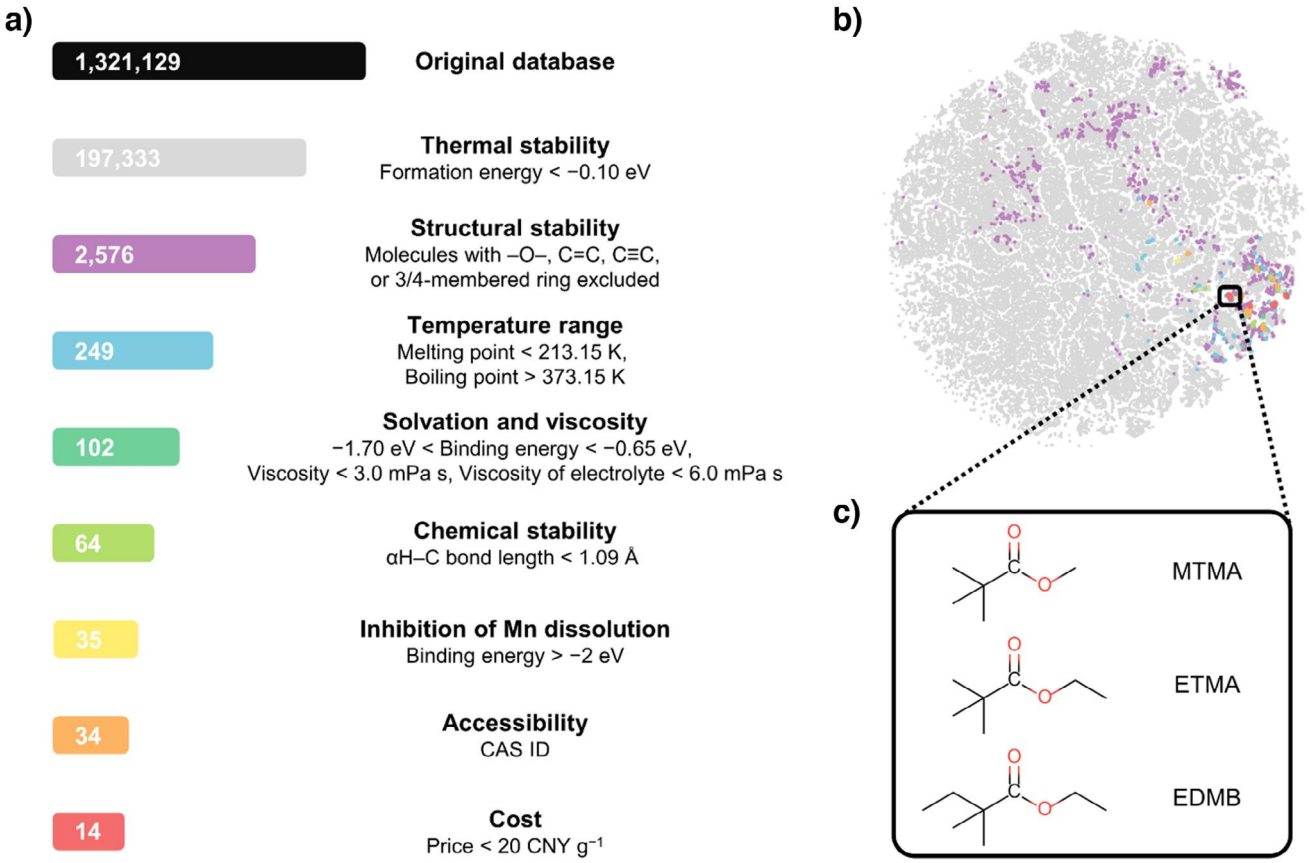

Figure 2. Design of molecules for high-temperature fast-charging lithium-ion battery electrolytes. a) Screening procedure based on requirements for physicochemical properties of molecules and electrolytes. b) Visualization of molecular representations for molecules in each screening step. c) Structural formulas of three recommended molecules, methyl trimethylacetate (MTMA), ethyl trimethylacetate (ETMA), and ethyl 2,2-dimethylbutanoate (EDMB), for further experimental verifications.

The chemical space of molecules in each screening step was further visualized in Figure 2b by *t*-distributed stochastic neighbor embedding (tSNE) method (clustering analysis in methods). The molecular distribution gradually converges into a concentrated region, which indicates that the selected molecules share similar structural features and properties. Three carboxylate molecules, i.e., MTMA, ETMA, and EDMB, that are readily available on the reagent platform were purchased and then assessed to validate their HTFC performances (Figure 2c).

Operating Voltage and Temperature Range of the Selected Solvents

To further verify the effectiveness of the above data–knowledge-dual-driven screening method, the electrochemical stability of the three predicted carboxylate molecules (MTMA, ETMA, and EDMB) was first characterized by both linear sweep voltammetry (LSV) and electrochemical floating tests (electrolyte formulas supplied in materials and electrolytes). Meanwhile, routine carbonates, EC and DMC, were selected as control samples. As expected, EC and DMC exhibit inferior anodic stability with an increasing current starting smaller than 4.0 V (Figure 3a). In comparison, the anodic stability of carboxylates can increase to larger than 5.2 V. Especially, MTMA delivered the increasing current starting around 5.5 V, indicating its super compatibility with high-voltage cathodes. To further verify the practical oxidation stability of the carboxylate-based electrolytes, an electrochemical floating test was conducted in Li||NCM811 cells with potential ranging from 4.3 to 4.7 V (vs. Li/Li^+) in a step of 0.1 V. As a result, the ETMA- (1.5 M lithium bis(fluorosulfony)imide) (LiFSI) in ETMA/FEC/PS) and EDMB- (1.5 M LiFSI in EDMB/FEC/PS) based electrolytes remain stable with minimal leak current increase before the voltage reaches 4.7 V, whereas the MTMA- (1.5 M LiFSI in MTMA/FEC/PS) and EC/DMC- (1.0 M lithium hexafluorophosphate ($LiPF_6$) in EC/DMC) based electrolytes demonstrate a much larger leak current and rising polarization, particularly above 4.6 V (Figure S5). Additionally, the carboxylate-based electrolytes have excellent compatibility with the Li metal electrode, resulting in a high plating and stripping Coulombic efficiency (CE) of approximately 95%, in contrast to the fluctuant CE around 86% in EC/DMC-based electrolyte (Figure S6).

Beyond electrochemical stability, the electrochemical performances of four electrolytes under variant temperatures

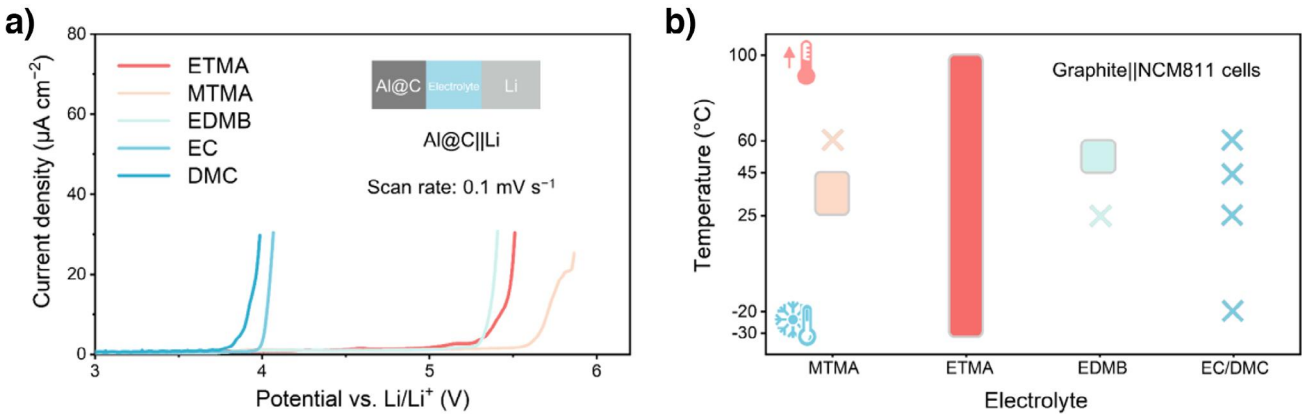

Figure 3. Anodic stability and operating temperature of cells. a) LSV anodic scanning in the Li||Al@C (carbon-coated Al) half cells at a scan rate of 0.1 mV^{-1}. b) The operating temperature range of the graphite||NCM811 full cells employing different electrolytes.

were evaluated in graphite||NCM811 (4.0 mAh cm^{-2}) cells (Figure 3b). Under 45 °C, the capacity of EC/DMC-based cells degraded very fast and only maintained 2.4 mAh cm^{-2} after 33 cycles at 0.5 C, indicating the extremely high requirements for electrolytes at high-temperature conditions (Figure S7A). Spectacularly, the cells employing ETMA- and EDMB-based electrolytes could stably work at high temperatures (0.5 C at 45 °C and 0.2 C at 60 °C, Figure S8). Especially, the cell using the ETMA-based electrolyte could even cycle at 100 °C (Figure S9), while the cell based on MTMA electrolyte could only afford the cell to work at 0.2 C and 45 °C (cell failure at higher temperatures or rates, Figure S7B). Although the boiling point of MTMA is much higher than the operating temperature of the cells, cells using MTMA-based electrolytes did not demonstrate sufficient high-temperature performance. This means that only relying on the boiling point of the solvent to correlate the high-temperature performance of the cells in the process of electrolyte screening procedure is not comprehensive. According to the above electrochemical performances, only ETMA and EDMB can match with high-temperature LIBs (Note S1 in Supporting Information).

However, when it comes to the room-temperature test (1.0 C at 25 °C), the EDMB-based electrolyte failed to retain capacity within 20 cycles. Moreover, the cell using EC/DMC-based electrolyte exhibited a capacity rollover induced by Li plating on graphite anode (Figures S10 and S11). By contrast, the cell using ETMA-based electrolytes exhibited outstanding performance with 97% capacity retention after 60 cycles. Despite structural similarities, the variation in carbon chain length among the three screened carboxylate molecules results in significant disparities in cell performance. After comprehensively considering the electrochemical performances at both room and high temperatures, ETMA was finally selected as the primary electrolyte solvent in the following, with the EC/DMC electrolyte still serving as the reference. In addition to its outstanding performance at high and room temperatures, the cells with ETMA-based electrolyte also surpass those utilizing EC/DMC electrolyte at low temperature (Note S2 and Figures S12–S14).

Characterization of Solvation Structures and Interfacial Chemistry

MD simulations were applied to investigate the solvation structure of both ETMA and EC/DMC electrolytes since the solvation structure acts as the precursor of electrode–electrolyte interphase (EEI), which determines the cycling stability and longevity of LIBs.[42–44] As a result of the solvation structures (>98% Li^+ bounding with one or more FSI^- anions and FEC molecules in the anion-rich Li^+ solvation structure of ETMA-based electrolyte, compared with <47% Li^+ coordinating with PF_6^- anions in solvation sheath of EC/DMC-based electrolyte, Note S3, Figures S15–S17), a great number of FSI^- and FEC molecules can be preferentially reduced to create a LiF-rich EEI in the ETMA-based electrolyte, while the carbonate solvents in the EC/DMC-based electrolyte tend to degrade first, resulting in the formation of a separate organic layer in the EEI.[45]

The structures of SEI formed in two electrolytes were resolved by time-of-flight secondary ion mass spectrometry (ToF-SIMs, in Figures S18 and S19). There are more ionic fragments of organic components ($C_2H_3O^-$, mainly decomposed from solvents)[46] detected priorly at the top surface of the SEI formed in EC/DMC-based electrolytes compared with that in the ETMA-based electrolyte. Meanwhile, the LiF inorganic constituents (LiF^-)[47] in the SEI derived from the ETMA-based electrolyte are distinctly richer than those in the EC/DMC-based electrolyte (Note S4). The above SEI structure in the ETMA-based electrolyte was further confirmed by cryo-transmission electron microscopy (cryo-TEM), where the interphase film covering the graphite is primarily composed of LiF (Figure S20). In addition, based on the fitting results of X-ray photoelectron spectroscopy (XPS) F 1s spectra with controlled sputtering time, the SEI in ETMA-based electrolyte exhibited more LiF and less C─F signals compared to the formed SEI in EC/DMC-based electrolyte (Figure S21), demonstrating distinctive electrolyte decomposition pathways and products leveraging from the unique solvation structure. Moreover, more inorganic components (Li_2O, Li_2S, Li_3N, etc.) were observed in

the interfacial film generated in the ETMA-based electrolyte (Figures S21–S23). Combining the evidence of ToF-SIMs, cryo-TEM, and XPS, a robust bilayer SEI with a LiF-rich inner layer and an organic-fewer outer layer was formed in the ETMA-based electrolyte. Furthermore, the inorganic ingredients that dominated the SEI in the ETMA-based electrolyte are effective in preventing side reactions and improving the cycle performance of cells. On the contrary, mainly solvent-induced SEI in the EC/DMC-based electrolyte is too deficient to ensure the battery cycle stability due to the insufficient interface stability. For instance, the SEI formed in the electrolyte containing ETMA has significantly lower levels of Mn^- fragments compared with that in the EC/DMC electrolyte (Figure S24), which agrees with the high-throughput screening presetting that the ETMA electrolyte is supposed to suppress the dissolution of transition metal from the NCM811 cathode.

The unique SEI structure formed in the ETMA electrolyte can decrease the activation energy of both Li^+ desolvation ($E_{a,ct}$) and Li^+ transport through SEI ($E_{a,SEI}$), which was further validated by temperature-dependent electrochemical impedance spectroscopy (EIS) with a three-electrode setup. The three-electrode system can monitor the impedance of the graphite anode without the interference of the Li counter electrode (Figure S25).[48] The $E_{a,ct}$ and $E_{a,SEI}$ were obtained by fitting the Arrhenius law (Figure S26). As a result, an obviously decreased Li^+ desolvation energy barrier was observed in ETMA-based electrolyte ($E_{a,ct} = 58.0$ kJ mol^{-1}) compared to EC/DMC-based electrolyte ($E_{a,ct} = 64.0$ kJ mol^{-1}), verifying the weaker Li^+–solvent interaction in the former. Most importantly, the activation energy of Li^+ transport through SEI in ETMA-based electrolyte ($E_{a,SEI} = 52.0$ kJ mol^{-1}) is significantly lower than in EC/DMC-based electrolyte ($E_{a,SEI} = 72.0$ kJ mol^{-1}), suggesting the rapid Li^+ diffusion among abundant phase boundaries in the inorganic SEI derived from ETMA-based electrolyte. The results of lowered desolvation barrier and inorganic species-dominated SEI imply that ETMA is promising to derive a robust SEI to passivate and insulate the graphite–electrolyte interface while ensuring a facile charge transfer and Li^+ transport process.

Evolution of Interfacial Chemistry at High Temperature

An elevated temperature (especially above 45 °C) will dramatically accelerate the decomposition reactions of the electrolyte, resulting in a rise in the content of organic products in the EEI and also the interfacial impedance. The ex situ EIS of graphite||NCM811 cells cycled at 45 °C was analyzed. The semicircles in the high- and intermediate-frequency regions of EIS represent the resistance of interphasial film (resistance of cathode electrolyte interphase + resistance of solid electrolyte interphase, $R_{CEI} + R_{SEI}$) and the charge transfer resistance (R_{ct}), respectively. The total resistance, as a sum of $R_{CEI} + R_{SEI}$ and R_{ct}, is denoted by R_{sum}. For the cells employing the EC/DMC-based electrolyte, R_{sum} doubles from the 1st cycle to the 50th cycle, particularly due to the increase in resistance of $R_{CEI} + R_{SEI}$ (Figure S27A). However, the R_{sum} value in the cell with the ETMA-based electrolyte is maintained at a constant level (Figure S27B). To decouple the intertwined interfacial impedance of the cathode and anode, the distribution of relaxation times (DRT) was thereafter used for impedance resolution based on the corresponding time constants (τ) of the electrochemical steps.[49,50] As depicted in Figure 4a, in the EC/DMC-based electrolyte, the interfacial impedance at 45 °C is primarily influenced by R_{SEI}, while R_{CEI} only shows a slight increase during 50 cycles (Figure S27C,D and Table S2). Specifically, the R_{SEI} has been steadily increasing, from 2.4 Ω after the first cycle to 62.2 Ω after the 25th cycle and then to 72.4 Ω after the 50th cycle, with an over 30-fold increment during the high-temperature test. In contrast, the R_{CEI} and R_{SEI} of the ETMA-based electrolyte are both almost unchanged (ca. 4.0 Ω) within 50 cycles at 45 °C, benefiting from its stable interfacial chemistry.

Subsequently, a postmortem analysis was performed on graphite anodes obtained from the cycled cells at a temperature of 45 °C. The scanning electron microscope (SEM) images demonstrate that the graphite anode matched with the EC/DMC-based electrolyte is covered by thick deposits (Figure 4b and Figure S28), and it is hard to distinguish the gaps between graphite particles. The apparent depositions above graphite particles can trigger rapid degradation in cell performance by hindering Li^+ diffusion to the interior of the active materials and consuming Li inventory due to the persistent interfacial side reactions. In contrast, clean and well-defined graphite particles can be observed on the anode matched with the ETMA-based electrolyte after 50 cycles at 45 °C. Such reduced electrodeposits on the graphite anode cycling at high temperatures reflect that the SEI derived from anion-rich solvation structures works well in insulating electron tunneling and resulting side reactions.

To analyze the composition of the deposited layer on cycled graphite anodes under 45 °C, XPS with an argon ion (Ar^+) sputtering depth profiling was employed. After the high-temperature cycling, the top surfaces of SEI in the two electrolytes are composed of organic species (C—F, C—O, and C═O), with high C, O element proportions at the 0 s sputtering time (Figures 4c,d and S29). In the F 1*s* spectra (Figure 4c), the SEI formed in EC/DMC-based electrolyte shows both LiF and C—F signals during sputtering process. In contrast, the LiF is stably detected as dominant peak in the SEI formed in ETMA-based electrolyte after 15 s sputtering time, along with more F concentration (three times greater than the value at 0 s) and N, S concentrations, which validates the inorganic inner SEI derived from FSI^- anion, FEC, and 1,3–PS co-solvents. Meanwhile, in the O 1*s* spectra (Figure 4d), the organic C—O and C═O species persist throughout the whole sputtering process in the SEI from the EC/DMC-based electrolyte, whereas the obviously inorganic Li_2O signals arise in the SEI formed in ETMA-based electrolyte after 15 s sputtering time. Overall, the inorganic LiF—Li_2O SEI derived from ETMA-based electrolyte enhances the high-temperature stability of the batteries while also preventing the decomposition of solvents and the deposition of organic products on the graphite anode, which results in the increase of interfacial resistance.

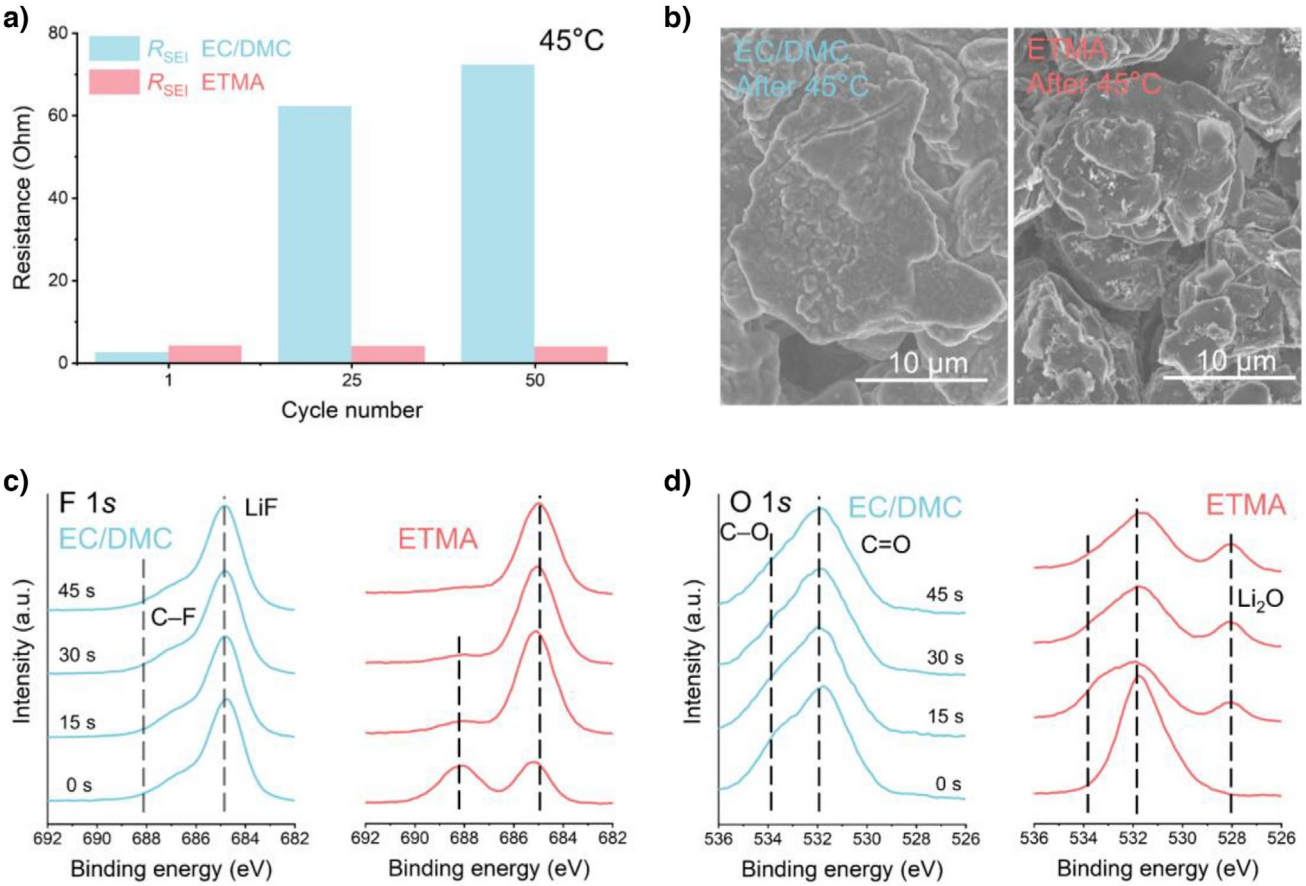

Figure 4. The evolution of interphasial chemistry and electrode morphology under 45 °C. a) The evolution of R_{SEI} in graphite||NCM811 full cells at 45 °C using EC/DMC- and ETMA-based electrolytes. b) SEM images of graphite electrodes harvested from graphite||NCM811 full cells with EC/DMC- and ETMA-based electrolyte after 50 cycles at 45 °C. c) and d) XPS spectra of the EC/DMC-generated and ETMA-derived SEI, with c) F 1s and d) O 1s of the SEIs on graphite electrodes after 50 cycles at 45 °C.

Electrochemical Performance of 4.3 V Graphite||NCM811 Pouch Cells

To validate the performance of the electrolytes in practical conditions, the graphite||NCM811 pouch cells were assembled and cycled under HTFC protocols. During the formation process, the gas generation of the ETMA-based electrolyte is negligible, indicating its super stability (Figure S30). What is more, the fast-charging performance of the pouch cell using the ETMA-based electrolyte outperforms that using the EC/DMC-based electrolyte at 45 °C (Figure 5a). Specifically, the cell using ETMA-based electrolyte shows a capacity retention of approximately 81% over 4100 cycles with 0.1 C reference performance test (RPT, herein, the current of C-rate is determined by the practical capacity of pouch cells, with current being equal to the product of nominal capacity and the applied rate) under 45 °C. Simultaneously, at 45 °C, pouch cell using electrolytes based on ETMA can acquire >80% capacity within 15 min of 4.0 C charging, while the cell with the EC/DMC-based electrolyte exhibits a significant deterioration during both fast-charging cycles and 0.1 C RPT. Even after 4100 fast-charging cycles, the cell employing the ETMA-based electrolyte in HTFC can still be charged to >60% capacity within 15 min. Furthermore, the corresponding cycled graphite anodes in different electrolytes are shown in Figure 5b. Severe Li plating was observed on the graphite anode and separator from the cell employing the EC/DMC-based electrolyte after 400 HFC cycles (Figure S31A). Nevertheless, the graphite anode in the ETMA-based electrolyte demonstrates palpable inhibition of Li plating, indicating the enhancement of SEI stability and interfacial kinetics during HTFC (Figure S31B). Moreover, the evolution of the pouch cell energy density during HFC is benchmarked against the United States Department of Energy (USDOE) target, which stipulates the 20% loss within 500 HFC cycles for a 180 Wh kg^{-1} cell (the dashed line in Figure 5c). The cell with the ETMA-based electrolyte has an initial energy density of 181 Wh kg^{-1} and retains 94.3% capacity over 500 cycles (only 5.7% loss) and 77.3% capacity after 4100 cycles, which greatly exceeds the USDOE target.

To further verify the high-temperature stability of pouch cells, cells with different electrolytes were tested at both 60 and 80 °C. Figure 5d compares the performance of graphite||NCM811 full cells in two electrolytes at 60 °C, where the cell using the ETMA-based electrolyte maintains approximately 82% capacity retention after 760 cycles at

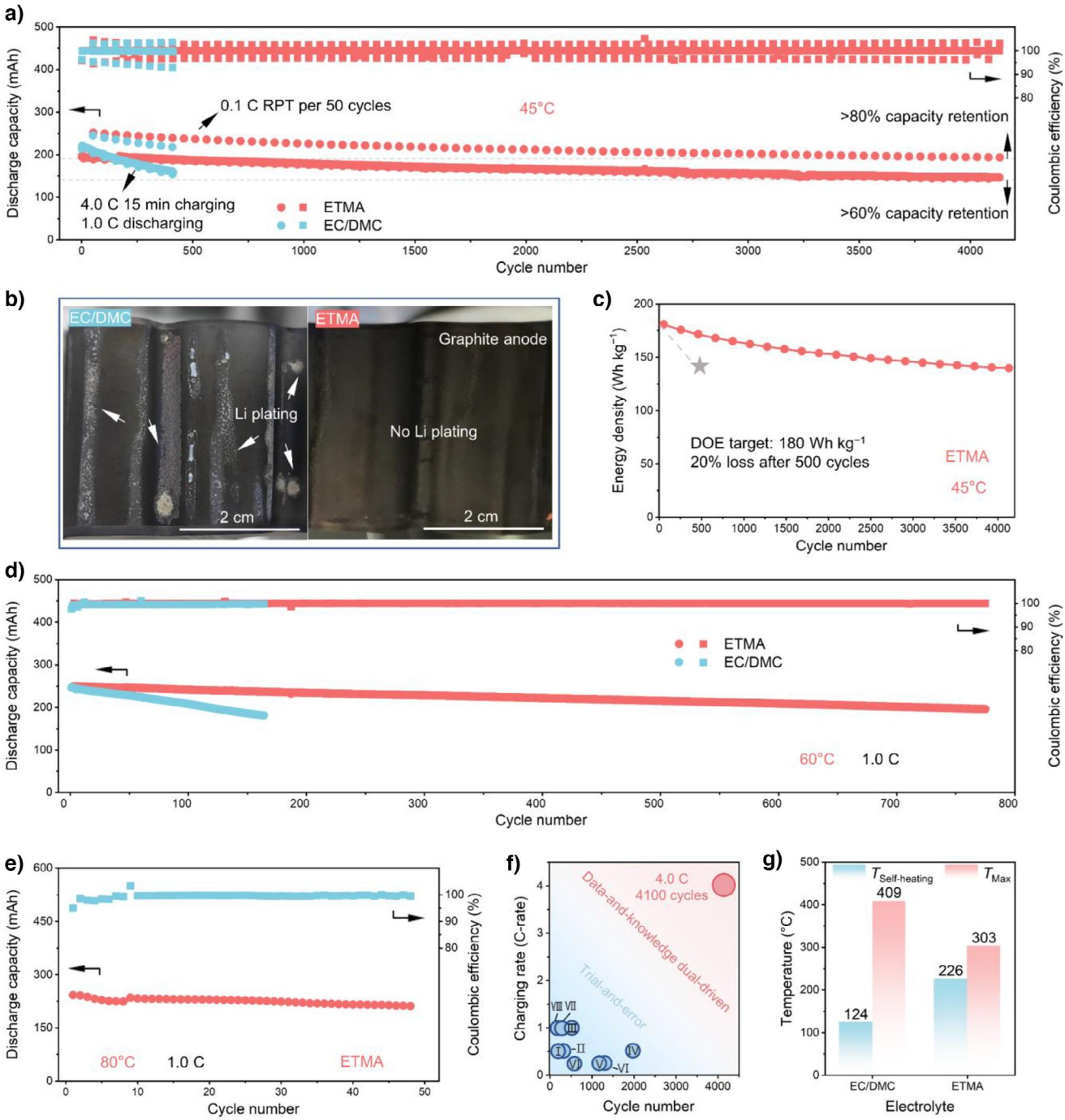

Figure 5. Electrochemical performance and thermal safety of pouch cells. a) Cycling performance of graphite||NCM811 pouch cells at 45 °C and 4.0 C (pouch cells were charged at 4.0 C in a CCCV mode for a fixed time of 15 min and then discharged at 1.0 C within 0.1 C RPT per 50 cycles). b) Optical images of graphite anodes cycled in EC/DMC and ETMA-based electrolyte. c) Energy density retention of the ETMA-based cell during 4.0 C (15 min, time termination) charging. d) and e) Electrochemical performance of the pouch cell containing different electrolytes at 60 °C d) and 85 °C e). f) The state-of-the-art performance comparison of commercial prismatic/pouch/cylindrical cells with more than 40 and 100 cycles in published literature and this work. The numbers of Roman numerals (1–8) correspond to Refs. [52–59]. g) The self-heating and maximum temperature of pouch cells in ARC tests with different electrolytes.

1.0 C. However, a fast capacity decay was observed in the cell utilizing the EC/DMC-based electrolyte, which reached its 80% nominal capacity retention within 135 cycles. Even at 80 °C, the cell based on the ETMA showed superior performance to that based on the EC/DMC electrolyte that the former can run for approximately 50 cycles, while the latter failed to operate at such a high temperature (Figure 5e). These results all suggest the high-temperature stability of the ETMA-based electrolyte enabled by the corresponding thermostable interfacial chemistry, compared

with conventional EC/DMC-based electrolytes and previous reports.[31,51]

Concerns about the long-term storage, fast kinetics, and safety of LIBs have led researchers to seek practical battery chemistries at extreme temperatures. Among the very few references that reported high-temperature performances (>40 °C and >100 cycles) of LIBs, only those employing pouch or cylindrical cells and summarizing their performance metrics, including charging rate and cycle number (terminating at ~~80% capacity retention), were selected (Figure 5f).[52–59] Given the intensified side reactions induced by high temperatures, major studies focused on cells cycling at a low voltage (<4.2 V, or using $LiFePO_4$-based cathode with a voltage below 3.7 V) and a low charging rate (<1.0 C) for prolonging the cell lifespan. Nevertheless, the data–knowledge-dual-driven designed ETMA-based cell in this work presents an astounding performance in a multi-index and comprehensive way with the highest voltage (4.3 V), the highest charging rate (4.0 C), and the longest cycle life (over 4100 cycles) compared with literature reports. In addition to the astounding performance of HTFC, the cells employing ETMA-based electrolyte also worked well at low temperatures, even at −60 °C (Note S5 and Figure S32).

The adiabatic rate calorimeter (ARC) tests further demonstrate the enhancement of the thermal stability of the ETMA-based electrolyte (Figures 5g and S33). Notably, $T_{\text{self-heating}}$, the self-heating rate of the battery >0.02 °C min^{-1} during thermal runaway, suggests that the exothermic reaction inside the battery will begin to elevate the temperature of the battery automatically. The higher $T_{\text{self-heating}}$ of LIB employing ETMA-based electrolyte (226 °C) compared with that with the EC/DMC-based electrolyte (124 °C) certifies the slower side reaction rate, which proves the palpable interfacial stability leveraging on the interphase components derived from the ETMA-based electrolyte. When the heat generation inside the battery is superimposed with progressing reactions, the battery will reach the maximum temperature of thermal runaway, T_{Max}. The T_{Max} of thermal runaway reduces from 409 to 303 °C, by replacing the EC/DMC-based electrolyte with the ETMA-based electrolyte. These results further prove that the thermal safety of the LIBs can be improved by enhancing the thermal stability of interfacial film through the electrolyte design.

Conclusion

Three carboxylate-based solvent molecules were screened from more than 1.3 million molecules through a knowledge–data-dual-driven approach, which is embedded with the parameterized properties required for HTFC. Compared with commercial carbonate-based electrolytes, the as-designed ETMA-based electrolyte achieved stable HTFC ability (>4100 cycles at 4.0 C and 45 °C) and high thermal safety in pouch cells ($T_{\text{self-heating}}$ and T_{max} in thermal runaway of the ETMA electrolyte were increased and decreased by 100 °C, respectively). This work not only revolutionizes the conventional approach to electrolyte design and solvent screening in HTFC applications but also proves the advantages of embedding domain knowledge into data-driven and machine-learning methodologies.

Acknowledgements

This work was supported by the National Key Research and Development Program (2021YFB2500300), the Beijing Municipal Natural Science Foundation (L233004 and L247015), the National Natural Science Foundation of China (T2322015, 22109007, 22393900, 22109011, 52394170, 52394171, 22109086, 22209010, and 22108151), and the Tsinghua University Initiative Scientific Research Program. The authors thank Dr. R. Xu (graduated from the Beijing Institute of Technology) for insightful discussion regarding the experiments.

Conflict of Interests

The authors declare no conflict of interest.

Data Availability Statement

The data that support the findings of this study are available from the corresponding author upon reasonable request.

Keywords: Data–knowledge-dual-driven screening · Fast charging · High temperature · Lithium-ion batteries · Molecular design

[1] M. Li, J. Lu, Z. Chen, K. Amine, *Adv. Mater.* **2018**, *30*, e1800561.
[2] Z. P. Cano, D. Banham, S. Y. Ye, A. Hintennach, J. Lu, M. Fowler, Z. W. Chen, *Nat. Energy* **2018**, *3*, 279–289.
[3] X. Q. Zeng, M. Li, D. A. El-Hady, W. Alshitari, A. S. Al-Bogami, J. Lu, K. Amine, *Adv. Energy Mater.* **2019**, *9*, 1900161.
[4] J. Deng, C. Bae, A. Denlinger, T. Miller, *Joule* **2020**, *4*, 511–515.
[5] A. Tomaszewska, Z. Chu, X. Feng, S. O'Kane, X. Liu, J. Chen, C. Ji, E. Endler, R. Li, L. Liu, Y. Li, S. Zheng, S. Vetterlein, M. Gao, J. Du, M. Parkes, M. Ouyang, M. Marinescu, G. Offer, B. Wu, *eTrans* **2019**, *1*, 100011.
[6] G.-L. Zhu, C.-Z. Zhao, J.-Q. Huang, C. X. He, J. Zhang, S. H. Chen, L. Xu, H. Yuan, Q. Zhang, *Small* **2019**, *15*, 1805389.
[7] M. Li, M. Feng, D. Luo, Z. Chen, *Cell. Rep. Phys. Sci.* **2020**, *1*, 100212.
[8] L. L. Lu, Y. Y. Lu, Z. X. Zhu, J. X. Shao, H. B. Yao, S. G. Wang, T. W. Zhang, Y. Ni, X. X. Wang, S. H. Yu, *Sci. Adv.* **2022**, *8*, eabm6624.
[9] H. Jin, S. Xin, C. Chuang, W. Li, H. Wang, J. Zhu, H. Xie, T. Zhang, Y. Wan, Z. Qi, W. Yan, Y. R. Lu, T. S. Chan, X. Wu, J. B. Goodenough, H. Ji, X. Duan, *Science* **2020**, *370*, 192–197.
[10] X.-G. Yang, T. Liu, Y. Gao, S. Ge, Y. Leng, D. Wang, C.-Y. Wang, *Joule* **2019**, *3*, 3002–3019.
[11] C.-Y. Wang, T. Liu, X.-G. Yang, S. Ge, N. V. Stanley, E. S. Rountree, Y. Leng, B. D. McCarthy, *Nature* **2022**, *611*, 485–490.
[12] S. Tu, B. Zhang, Y. Zhang, Z. Chen, X. Wang, R. Zhan, Y. Ou, W. Wang, X. Liu, X. Duan, L. Wang, Y. Sun, *Nat. Energy* **2023**, *8*, 1365–1374.
[13] K.-H. Chen, V. Goel, M. J. Namkoong, M. Wied, S. Müller, V. Wood, J. Sakamoto, K. Thornton, N. P. Dasgupta, *Adv. Energy Mater.* **2021**, *11*, 2003336.

[14] Y.-X. Yao, X. Chen, N. Yao, J.-H. Gao, G. Xu, J.-F. Ding, C.-L. Song, W.-L. Cai, C. Yan, Q. Zhang, *Angew. Chem. Int. Ed.* **2023**, *62*, e202214828.
[15] S. Ahmed, I. Bloom, A. N. Jansen, T. Tanim, E. J. Dufek, A. Pesaran, A. Burnham, R. B. Carlson, F. Dias, K. Hardy, M. Keyser, C. Kreuzer, A. Markel, A. Meintz, C. Michelbacher, M. Mohanpurkar, P. A. Nelson, D. C. Robertson, D. Scoffield, M. Shirk, T. Stephens, R. Vijayagopal, J. Zhang, *J. Power Sources* **2017**, *367*, 250–262.
[16] M. Keyser, A. Pesaran, Q. Li, S. Santhanagopalan, K. Smith, E. Wood, S. Ahmed, I. Bloom, E. Dufek, M. Shirk, A. Meintz, C. Kreuzer, C. Michelbacher, A. Burnham, T. Stephens, J. Francfort, B. Carlson, J. Zhang, R. Vijayagopal, K. Hardy, F. Dias, M. Mohanpurkar, D. Scoffield, A. N. Jansen, T. Tanim, A. Markel, *J. Power Sources* **2017**, *367*, 228–236.
[17] X. Lin, M. Salari, L. M. Arava, P. M. Ajayan, M. W. Grinstaff, *Chem. Soc. Rev.* **2016**, *45*, 5848–5887.
[18] T. Taskovic, A. Eldesoky, C. P. Aiken, J. R. Dahn, *J. Electrochem. Soc.* **2022**, *169*, 100547.
[19] K. Q. Qin, S. H. Ge, N. Gupta, T. Sasaki, C. Y. Wang, *J. Power Sources* **2025**, *630*, 236094.
[20] R. S. Longchamps, X. G. Yang, C. Y. Wang, *ACS Energy Lett.* **2022**, *7*, 1103–1111.
[21] P. Liu, L. Yang, B. Xiao, H. Wang, L. Li, S. Ye, Y. Li, X. Ren, X. Ouyang, J. Hu, F. Pan, Q. Zhang, J. Liu, *Adv. Funct. Mater.* **2022**, *32*, 2208586.
[22] S. S. Zhang, *InfoMat* **2021**, *3*, 125–130.
[23] D. Zhang, L. Li, W. Zhang, M. Cao, H. Qiu, X. Ji, *Chin. Chem. Lett.* **2023**, *34*, 107122.
[24] E. R. Logan, D. S. Hall, M. M. E. Cormier, T. Taskovic, M. Bauer, I. Hamam, H. Hebecker, L. Molino, J. R. Dahn, *J. Phys. Chem. C* **2020**, *124*, 12269–12280.
[25] X. Huang, R. Li, C. Sun, H. Zhang, S. Zhang, L. Lv, Y. Huang, L. Fan, L. Chen, M. Noked, X. Fan, *ACS Energy Lett.* **2022**, *7*, 3947–3957.
[26] H. Cheng, Z. Ma, P. Kumar, H. Liang, Z. Cao, H. Xie, L. Cavallo, H. Kim, Q. Li, Y.-K. Sun, J. Ming, *Adv. Energy Mater.* **2024**, *14*, 2304321.
[27] D. Lu, R. Li, M. M. Rahman, P. Yu, L. Lv, S. Yang, Y. Huang, C. Sun, S. Zhang, H. Zhang, J. Zhang, X. Xiao, T. Deng, L. Fan, L. Chen, J. Wang, E. Hu, C. Wang, X. Fan, *Nature* **2024**, *627*, 101–107.
[28] S. J. Yang, N. Yao, F. N. Jiang, J. Xie, S. Y. Sun, X. Chen, H. Yuan, X. B. Cheng, J. Q. Huang, Q. Zhang, *Angew. Chem. Int. Ed.* **2022**, *61*, e202214545.
[29] J. Wang, Y. Yamada, K. Sodeyama, E. Watanabe, K. Takada, Y. Tateyama, A. Yamada, *Nat. Energy* **2017**, *3*, 22–29.
[30] X. G. Yang, T. Liu, C. Y. Wang, *Nat. Energy* **2021**, *6*, 176–185.
[31] J. Liao, R. S. Longchamps, B. D. Mccarthy, F. F. Shi, C. Y. Wang, *ACS Energy Lett.* **2024**, *9*, 771–778.
[32] J. Xu, J. Zhang, T. P. Pollard, Q. Li, S. Tan, S. Hou, H. Wan, F. Chen, H. He, E. Hu, K. Xu, X. Q. Yang, O. Borodin, C. Wang, *Nature* **2023**, *614*, 694–700.
[33] J. Zhang, H. Zhang, S. Weng, R. Li, D. Lu, T. Deng, S. Zhang, L. Lv, J. Qi, X. Xiao, L. Fan, S. Geng, F. Wang, L. Chen, M. Noked, X. Wang, X. Fan, *Nat. Commun.* **2023**, *14*, 2211.
[34] D.-J. Yoo, Q. Liu, O. Cohen, M. Kim, K. A. Persson, Z. Zhang, *Adv. Energy Mater.* **2023**, *13*, 2204182.
[35] K. Xu, *Chem. Rev.* **2004**, *104*, 4303–4418.
[36] K. Xu, *Chem. Rev.* **2014**, *114*, 11503–11618.
[37] B. D. McKay, M. A. Yirik, C. Steinbeck, *J. Cheminform.* **2022**, *14*, 24.
[38] Y.-C. Gao, Y.-H. Yuan, S. Huang, N. Yao, L. Yu, Y.-P. Chen, Q. Zhang, X. Chen, *Angew. Chem. Int. Ed.* **2025**, *64*, e202416506.
[39] O. P. Korobeinichev, S. B. Ilyin, T. A. Bolshova, V. M. Shvartsberg, A. A. Chernov, *Combust. Flame* **2000**, *121*, 593–609.
[40] C. Wang, L. D. Xing, J. Vatamanu, Z. Chen, G. Y. Lan, W. S. Li, K. Xu, *Nat. Commun.* **2019**, *10*, 3423.
[41] Q. Q. Ren, Y. F. Yuan, S. Wang, *ACS Appl. Mater. Interfaces* **2022**, *14*, 23022–23032.
[42] Y. Yang, C. Yan, J. Q. Huang, *Acta Phys. Chim. Sin.* **2021**, *37*, 2010076–2010089.
[43] Y. Yang, L. Xu, C. Yan, J.-Q. Huang, Q. Zhang, *Energy Lab.* **2022**, *1*, 220011.
[44] C. Yan, R. Xu, Y. Xiao, J. F. Ding, L. Xu, B. Q. Li, J. Q. Huang, *Adv. Funct. Mater.* **2020**, *30*, 1909887.
[45] Y. X. Yao, X. Chen, C. Yan, X. Q. Zhang, W. L. Cai, J. Q. Huang, Q. Zhang, *Angew. Chem. Int. Ed.* **2021**, *60*, 4090–4097.
[46] Y. Mo, G. Liu, J. Chen, X. Zhu, Y. Peng, Y. Wang, C. Wang, X. Dong, Y. Xia, *Energy Environ. Sci.* **2024**, *17*, 227–237.
[47] Q. K. Zhang, X. Q. Zhang, J. Wan, N. Yao, T. L. Song, J. Xie, L. P. Hou, M. Y. Zhou, X. Chen, B. Q. Li, R. Wen, H. J. Peng, Q. Zhang, J. Q. Huang, *Nat. Energy* **2023**, *8*, 725–735.
[48] Y. X. Yao, N. Yao, X. R. Zhou, Z. H. Li, X. Y. Yue, C. Yan, Q. Zhang, *Adv. Mater.* **2022**, *34*, e2206448.
[49] Z. Li, Y. X. Yao, M. Zheng, S. Sun, Y. Yang, Y. Xiao, L. Xu, C. B. Jin, X. Y. Yue, T. Song, P. Wu, C. Yan, Q. Zhang, *Angew. Chem. Int. Ed.* **2025**, *64*, e202409409.
[50] R. Huang, X. Wang, B. Jiang, S. Chen, G. Zhang, J. Zhu, X. Wei, H. Dai, *J. Power Sources* **2023**, *566*, 232929.
[51] S. H. Ge, Y. J. Leng, T. Liu, R. S. Longchamps, X. G. Yang, Y. Gao, D. W. Wang, D. H. Wang, C. Y. Wang, *Sci. Adv.* **2020**, *6*, eaay7633.
[52] L. Chen, J. H. Lu, Y. B. Wang, P. He, S. B. Huang, Y. Liu, Y. Z. Wu, G. P. Cao, L. Wang, X. M. He, J. Y. Qiu, H. Zhang, *Energy Storage Mater.* **2022**, *49*, 493–501.
[53] Y. Q. Chen, Q. He, Y. Mo, W. Zhou, Y. Zhao, N. Piao, C. Liu, P. T. Xiao, H. Liu, B. H. Li, S. Chen, L. Wang, X. M. He, L. D. Xing, J. L. Liu, *Adv. Energy Mater.* **2022**, *12*, 2201631.
[54] Y. L. Zhu, J. G. Zhu, B. Jiang, X. Y. Wang, X. Z. Wei, H. F. Dai, *J. Energy Storage* **2023**, *60*, 106624.
[55] S. H. Ge, R. S. Longchamps, T. Liu, J. Liao, Y. J. Leng, C. Y. Wang, *Cell Rep. Phys. Sci.* **2021**, *2*, 100584.
[56] C. P. Aiken, T. Taskovie, J. R. Dahn, *J. Electrochem. Soc.* **2022**, *169*, 090523.
[57] K. Tuul, S. Martin-Maher, C. Floras, W. Black, T. Taskovic, S. Chisholm, A. Clarke, E. Lust, J. R. Dahn, *J. Electrochem. Soc.* **2024**, *171*, 040510.
[58] Y. G. Zou, Z. Ma, G. Liu, Q. Li, D. M. Yin, X. J. Shi, Z. Cao, Z. N. Tian, H. Kim, Y. J. Guo, C. S. Sun, L. Cavallo, L. M. Wang, H. N. Alshareef, Y. K. Sun, J. Ming, *Angew. Chem. Int. Ed.* **2023**, *62*, e202216189.
[59] X. Y. Zheng, Z. Cao, W. Luo, T. Zhao, Y. Han, H. Yang, X. Y. Liu, Y. Zhou, J. Y. Wen, Y. Shen, H. H. Zheng, Y. H. Huang, *Adv. Funct. Mater.* **2023**, *33*, 2301550.

Manuscript received: March 05, 2025
Revised manuscript received: April 07, 2025
Accepted manuscript online: April 07, 2025
Version of record online: April 17, 2025